



Breezing through the Space Environment of Barnard's Star b

Julián D. Alvarado-Gómez^{1,6} , Cecilia Garraffo^{1,2,6} , Jeremy J. Drake¹ , Benjamin P. Brown³ , Jeffrey S. Oishi⁴ ,
Sofia P. Moschou¹ , and Ofer Cohen⁵ 

¹ Center for Astrophysics|Harvard & Smithsonian, 60 Garden Street, Cambridge, MA 02138, USA; jalvarad@cfa.harvard.edu, cgarraffo@cfa.harvard.edu

² Institute for Applied Computational Science, Harvard University, Cambridge, MA 02138, USA

³ Department of Astrophysical and Planetary Sciences, Laboratory for Atmospheric and Space Physics, University of Colorado at Boulder, 3665 Discovery Drive, Boulder, CO 80303, USA

⁴ Department of Physics and Astronomy Bates College, Carnegie Science Hall, 2 Andrews Road, Lewiston, ME, 04240, USA

⁵ University of Massachusetts at Lowell, Department of Physics & Applied Physics, 600 Suffolk Street, Lowell, MA 01854, USA

Received 2018 December 31; revised 2019 March 19; accepted 2019 March 28; published 2019 April 15

Abstract

A physically realistic stellar wind model based on Alfvén wave dissipation has been used to simulate the wind from Barnard's Star and to estimate the conditions at the location of its recently discovered planetary companion. Such models require knowledge of the stellar surface magnetic field that is currently unknown for Barnard's Star. We circumvent this by considering the observed field distributions of three different stars that constitute admissible magnetic proxies of this object. Under these considerations, Barnard's Star b experiences less intense wind pressure than the much more close-in planet Proxima b and the planets of the TRAPPIST-1 system. The milder wind conditions are more a result of its much greater orbital distance rather than in differences in the surface magnetic field strengths of the host stars. The dynamic pressure experienced by the planet is comparable to present-day Earth values, but it can undergo variations by factors of several during current sheet crossings in each orbit. The magnetopause standoff distance would be $\sim 20\%$ – 40% smaller than that of the Earth for an equivalent planetary magnetic field strength.

Key words: planets and satellites: terrestrial planets – stars: activity – stars: individual (Barnard's Star) – stars: late-type – stars: winds, outflows

1. Introduction

The detection by Ribas et al. (2018) of a planet around Barnard's Star is an important step in our growing understanding of the nature of planetary systems in the universe. The M3 V red dwarf Barnard's Star is the closest single star planetary system to the Sun.

Barnard's Star b (BSb) orbits at a distance similar to that of Mercury around the Sun. Ribas et al. (2018) note that the planet resides close to the snow line of Barnard's Star, where stellar irradiation is sufficiently weak to allow volatile elements to condense (Kennedy & Kenyon 2008). This characteristic renders BSb of special interest from the perspective of planet formation. There is growing agreement on the importance of the snow line region as a natal site of planetesimal formation and growth (e.g., Stevenson & Lunine 1988; Morbidelli et al. 2015; Mulders et al. 2015) and BSb promises to be an important keystone object for future progress.

Of more immediate interest is the potential of BSb for understanding planetary atmospheric evolution. It has an orbital semimajor axis of ~ 0.4 au, which is sufficiently wide, that it can be disentangled from the stellar signal and will be amenable to detailed study and direct imaging by next generation instrumentation (Trauger et al. 2016). This will allow the planetary atmosphere to be studied in unprecedented detail.

Several papers have pointed to the importance of extreme stellar activity and winds for understanding the evolution of planetary atmospheres around M dwarf stars (e.g., Lammer et al. 2009; Cohen et al. 2014; Vidotto et al. 2015; Garraffo et al. 2017). Magnetospheric and atmospheric evolution models are not yet able to predict how atmospheric initial conditions evolve under intense radiation environments. Nevertheless, progress has been made in this direction through 1D models of evaporating exoplanet atmospheres and stellar winds (Johnstone et al. 2015a, 2015b, 2015c). Based on detailed magnetohydrodynamic (MHD) modeling of the wind of Proxima Centauri, Garraffo et al. (2016) found that Proxima b is subject to dynamic wind pressures four orders of magnitude larger than Earth. The relatively long rotation period of Barnard's star of ~ 130 – 145 days (Benedict et al. 1998), combined with its modest present-day magnetic activity level (Toledo-Padrón et al. 2018), lead Ribas et al. (2018) to estimate an age of 7–10 Gyr for the system. BSb represents the outcome of planetary evolution over this long timescale through a history of strongly differing environmental conditions.

Here, we use detailed 3D MHD stellar wind models to examine the space weather conditions of the present-day Barnard's Star environment and investigate the influence of the stellar wind on its magnetosphere and atmosphere. Our wind models are driven by the observed magnetic field maps of three proxy stars, scaled to the expected range of surface field strength for Barnard's Star.

2. Methods

2.1. Corona and Stellar Wind

To simulate the environment in the Barnard's Star system, we employ the Space Weather Modeling Framework⁷ (SWMF;

⁶ These authors contributed equally to this work.

⁷ [Space Weather Modeling Framework](https://swmf.umd.edu/)

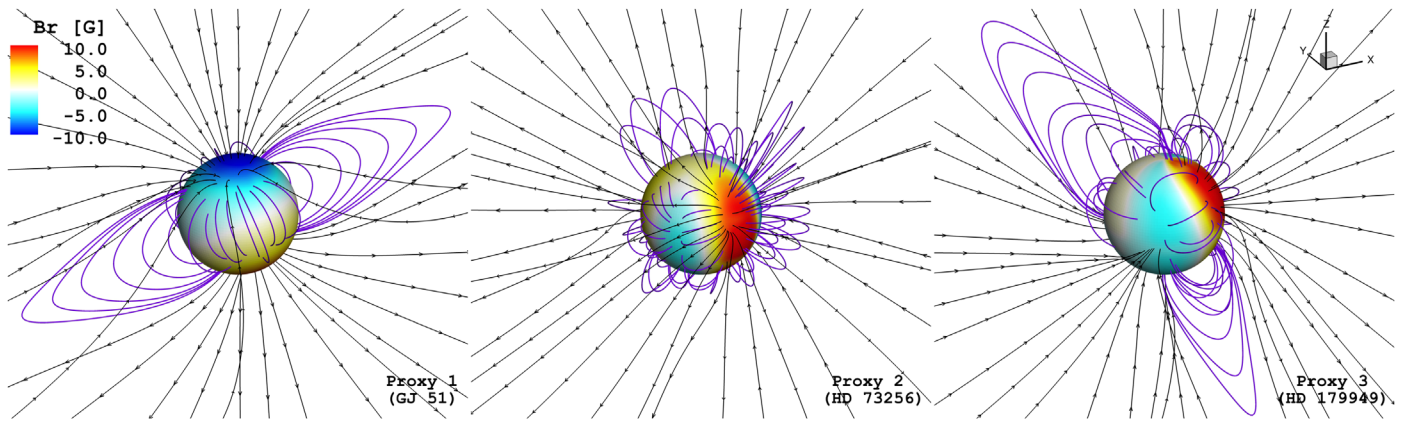


Figure 1. Inner boundary of our simulation domain, showing the large-scale ZDI radial magnetic field of three late-type stars driving the proxy models of Barnard’s Star (left: GJ 51, Morin et al. 2010; middle: HD 73256, Fares et al. 2013; right: HD 179949, Fares et al. 2012). The field strengths have been scaled to the indicated range. Selected closed (purple) and open (black) magnetic field lines are shown.

see Gombosi et al. 2018). In particular, we use the 3D MHD solver BATS-R-US (Tóth et al. 2012) and the Alfvén wave solar model (AWSoM; van der Holst et al. 2014). This model was developed to study the solar environment and has since been adapted and applied to astrophysical systems. It uses the distribution of the radial magnetic field on the surface of the star (magnetogram) as a boundary condition for the self-consistent calculation of the coronal heating and stellar wind acceleration due to Alfvén wave turbulent dissipation.

The AWSoM model assumes a non-ideal MHD regime, where the magnetically driven contributions are included as additional source terms in the energy and momentum equations, solved alongside the mass conservation and magnetic induction equations on a spherical grid. Radiative losses and electron heat conduction are also taken into account in the model. The simulation evolves until a steady-state solution is reached. Further details on the implementation and recent performance updates can be found in van der Holst et al. (2014) and Sokolov et al. (2016).

In previous studies we have used this code to simulate the space weather conditions around other M dwarf planet-hosting stars (e.g., Prox Cen, Garraffo et al. 2016; TRAPPIST-1, Garraffo et al. 2017). Unlike the Prox Cen or TRAPPIST-1 planets, the BSb orbit, with a semimajor axis of $a = 0.404 \pm 0.018$ au ($\sim 443.16 \pm 19.74 R_*$) and a relatively high eccentricity ($e = 0.32^{+0.10}_{-0.15}$), resides well outside the domain of the stellar corona. We use two coupled numerical domains which include the corona and wind acceleration region (the solar corona, or SC, module of the SWMF; $\sim 1\text{--}110 R_*$), and a wind propagation region (the inner heliosphere, or IH module; $105\text{--}750 R_*$) sufficiently large to enclose the maximum possible orbital separation of the planet. The non-ideal MHD effects described before are only considered in the SC domain, whose solution is then propagated into the IH ideal MHD scheme. A $5 R_*$ domain overlap is imposed to guarantee the robustness of the combined solution.

The IH domain utilizes adaptive mesh refinement for increased spatial discretization of regions with strong gradients in wind density occurring along the current sheet. The smallest cell size reached by our simulations in this domain is $\sim 1.46 R_*$ and consider more than 25 million spatial blocks. In the stellar context, this coupled modeling scheme has been employed to investigate the stellar wind properties in the habitable zones of Sun-like stars (see Alvarado-Gómez et al. 2016a, 2016b), and

this particular study represents its first application to the M dwarf regime.

2.2. Surface Magnetic Field

While high-resolution magnetograms are readily available for the Sun (e.g., from the *Solar and Heliospheric Observatory*⁸ and the *Solar Dynamics Observatory*⁹), for stars the only source of magnetograms at present is through spectropolarimetric observations and Zeeman–Doppler imaging (ZDI), which requires a minimum brightness and rotation velocity (Semel 1989; Donati et al. 1997). Unfortunately, with a visual magnitude of $V_{\text{mag}} = 9.511$ and a rotation period of ~ 130 days, the retrieval of a ZDI magnetic map of Barnard’s Star is currently unfeasible. As described by Reiners (2012), measurements in unpolarized light of the unsigned surface magnetic field strength via Zeeman broadening benefit from small rotational broadening. However, to our knowledge, there are no magnetic field measurements in the literature for Barnard’s Star using this technique.

Despite the lack of direct measurements, we can use information from previous studies to get a sense of the field strength and geometry expected for Barnard’s Star. On the one hand, X-ray luminosity is known to be strongly correlated with stellar rotation, and even more so with the Rossby number (Ro), defined as the rotation period (P_{rot}) over the convective turnover time (τ). Wright et al. (2011) used a sample of 725 Sun-like and later-type stars to calibrate this relationship. Interestingly, in two follow-up papers Wright & Drake (2016) and Wright et al. (2018) showed that this relationship also holds for fully convective stars like Barnard’s Star. Making use of this calibration, and the level of X-ray emission of Barnard’s Star ($\log L_X = 25.85$; Hünsch et al. 1999; Schmitt & Liefke 2004), we estimate $\tau \sim 120\text{--}150$ days, which results in $Ro \sim 0.9\text{--}1.2$.

Additionally, detailed numerical MHD convection models appropriate for fully convective stars have demonstrated that these objects are able to generate global-scale magnetic fields in their convection zones, despite the lack of a solar-like tachocline. In these simulations, especially at low Ro , significant magnetic energy has been found in the dipolar components of the field (Browning 2008; Yadav et al. 2015).

⁸ Solar and Heliospheric Observatory

⁹ Solar Dynamics Observatory

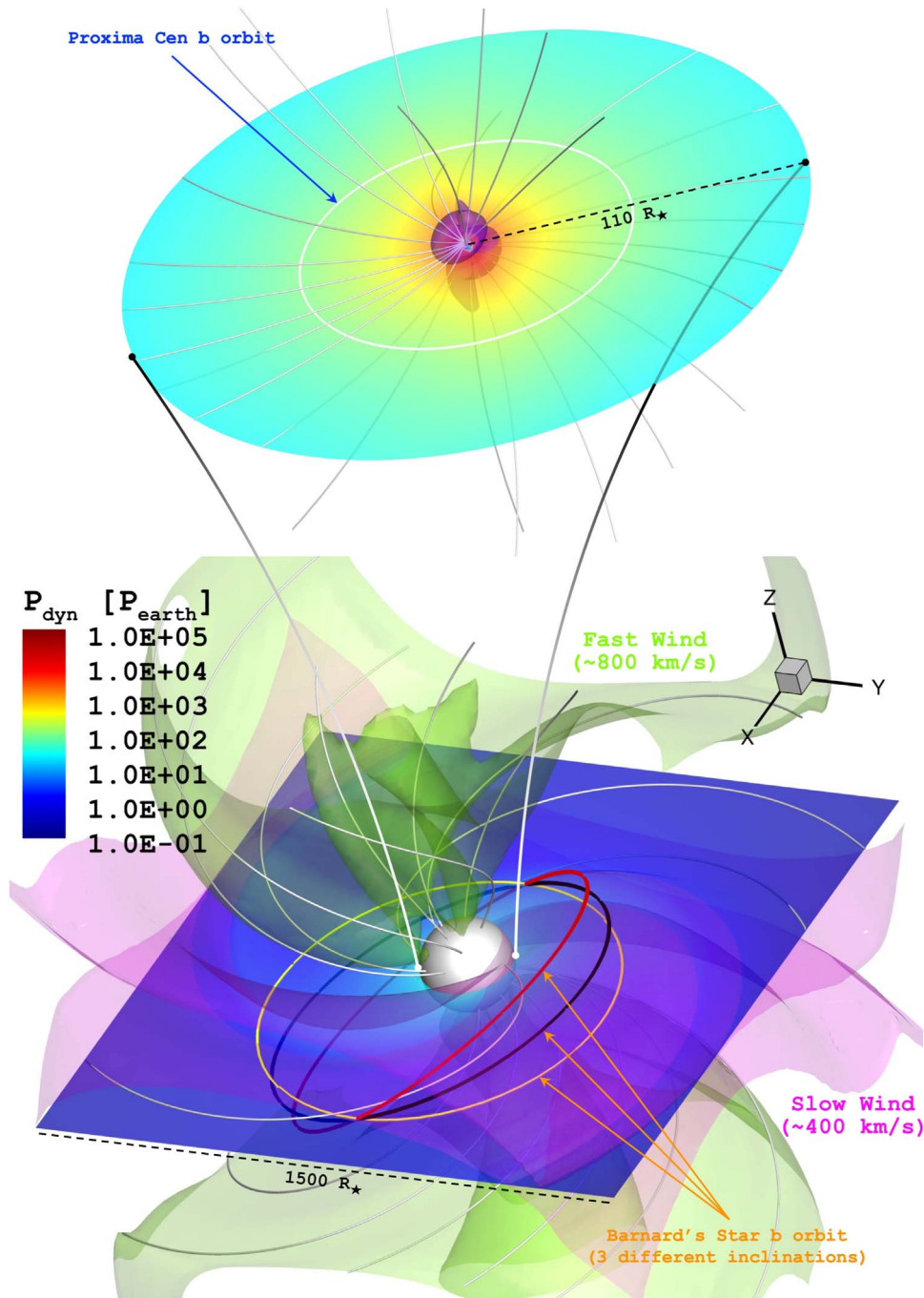


Figure 2. Multidomain numerical simulation of the stellar wind environment of Barnard’s Star, driven by the ZDI map of the proxy star GJ 51 (M5V). The top panel contains the stellar corona and wind acceleration region, extending from the surface of the star up to $110 R_*$. The Alfvén surface ($M_A = 1$) of the stellar wind is shown in purple (see the text for details). The wind solution is propagated to the extended domain presented in the bottom panel, which covers $1500 R_*$ in each cartesian direction and is centered in the star. Green and magenta isosurfaces delineate the boundaries of the resulting fast ($U_r \gtrsim 800 \text{ km s}^{-1}$) and slow ($U_r \lesssim 400 \text{ km s}^{-1}$) wind sectors. The color scale displays the wind dynamical pressure ($P_{\text{dyn}} = \rho U^2$), projected on the equatorial plane of both domains. The ellipses correspond to the orbit of BSb for three different inclination angles (0° , 15° , and 30°). The top panel also shows the orbit of Proxima Cen b for reference. Selected magnetic field lines are shown in white.

At higher Ro , the mean fields can continue to show strong dipole fractions even as the fluctuating fields increase in strength. In addition, spindown models predict dipole-dominated morphologies in these large Ro regimes (see Garraffo et al. 2018). In this context, we consider as one proxy for Barnard’s Star, the ZDI map of the star GJ 51 (Morin et al. 2010), which has a dipole-dominated geometry and similar spectral type (M5), albeit with a significantly shorter rotation

period (~ 1 day). This is the same magnetogram used in the study of the space weather of Proxima Cen by Garraffo et al. (2016) and allows us to perform a comparative analysis of the wind conditions around Proxima and Barnard’s Star.

Furthermore, from the compilation gathered by Vidotto et al. (2014), there are eight stars with $Ro > 0.9$, from which only four have published ZDI magnetic field maps: HD 78366 ($Ro \gtrsim 2.78$; Morgenthaler et al. 2011), HD 146233 ($Ro = 1.32$;

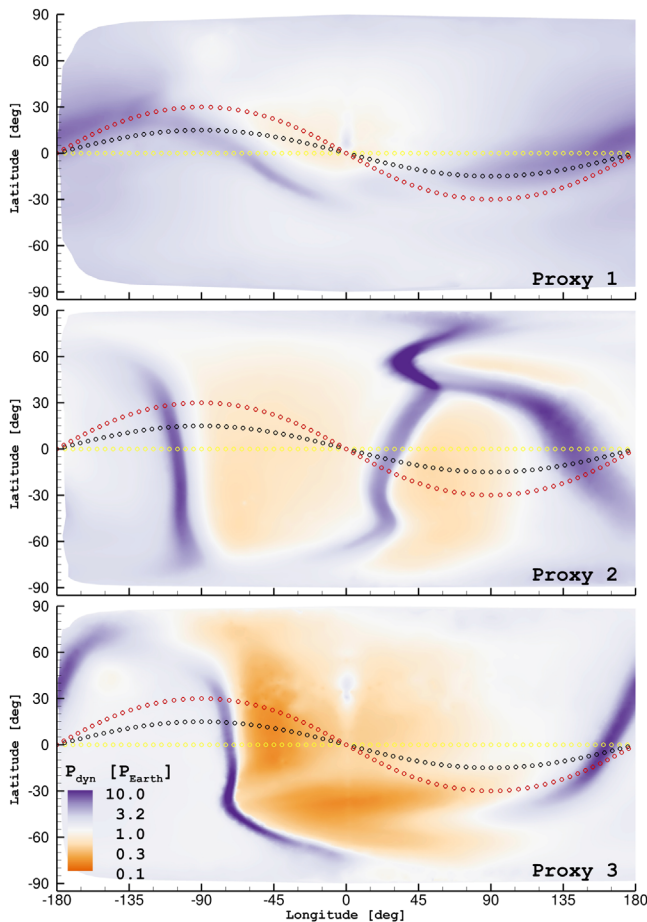


Figure 3. Mercator projection of the stellar wind dynamic pressure P_{dyn} , normalized to the solar wind pressure at 1 au, extracted from a spheroid containing possible orbits for BSb. The different panels show the results for each proxy simulation as indicated. Dotted lines in yellow, black, and red correspond to the 0° , 15° , and 30° inclination orbits, respectively (see Figure 2, bottom panel).

Petit et al. 2008), HD 73256 ($\text{Ro} = 0.96$; Fares et al. 2013), and HD 179949 ($\text{Ro} \gtrsim 1.72$; Fares et al. 2012). Both HD 73256 and HD 146233 are close to the estimated Ro values for Barnard’s Star and could serve as additional proxies for its field geometry. However, the resolution of the published ZDI map for the latter is too low for our numerical purposes. Therefore, we consider instead the map of HD 179949, which actually shows substantial similitude to the large-scale field of HD 146233. All maps considered here were taken directly from the publications (via an image–data transformation), and therefore they retain the intrinsic missing latitudes of ZDI observations.

The analysis of Vidotto et al. (2014) also indicates objects within the range of Ro estimated for Barnard’s Star, are expected to have an unsigned large-scale field between 1 and 10 G. For this reason, we have scaled the surface field strengths of all three of the different proxies to this range (Figure 1). Such a comparatively weak surface field is consistent with the very low level of activity measured for Barnard’s Star (Toledo-Padrón et al. 2018).

Finally, we stress that there are no ZDI maps for slowly rotating fully convective M dwarfs that could be used as even more suitable proxies of Barnard’s Star. By considering three different cases, we aim to cover observationally motivated possibilities in field geometry, and explore how these translate to the environment of the system. In this context, the results

presented here should be interpreted more as a global assessment of the range of variability of the stellar wind than absolute predictions for the system.

3. Results and Discussion

Figure 2 presents a composite visualization of the 3D stellar wind solution achieved for Barnard’s Star using the realistically scaled surface magnetic field map of GJ 51 (Figure 1, left panel). Both the SC and IH domains are shown, illustrating the way they are coupled in our simulations. We have performed similar wind simulations using the scaled ZDI maps of the other two proxy stars, HD 73256 and HD 179949 (Figure 1, middle and right panels). As part of the characterization of the stellar wind solution, we include the resulting Alfvén surface (AS), computed as the collection of points at which the Alfvénic Mach number¹⁰ is equal to one. The average size of the AS is similar in all cases, ranging between $8.2 R_*$ and $10.8 R_*$, placing BSb well within the super-Alfvénic regime of the stellar wind (as is the case for all solar system planets).

3.1. Mass-loss Rate

Before assessing the conditions experienced by the exoplanet, we first examine the results of the simulations in the context of stellar winds from cool main-sequence stars. The steady-state solutions reach maximum radial wind speeds (in km s^{-1}) of 863 (proxy 1), 800 (proxy 2), and 758 (proxy 3). The respective mass-loss rates in each case, expressed in solar units¹¹ (\dot{M}_\odot), are 0.085, 0.082, and 0.054.

In the absence of any observational constraints for the mass-loss rate from Barnard’s Star’s wind, we can use the \dot{M} constraints for other M dwarfs to compare with the values from our numerical models. Wood et al. (2001) reported an upper limit of $\dot{M} < 0.2 \dot{M}_\odot$ for Prox Cen, based on the astrospheric absorption signature appearing in the blue wing of the $\text{Ly}\alpha$ line. An independent 3σ upper limit of $\dot{M} < 14 \dot{M}_\odot$ ($\sim 3 \times 10^{-13} \dot{M}_\odot \text{ yr}^{-1}$) was obtained for this star by Wargelin & Drake (2002), using a more direct technique based on the X-ray signature resulting from stellar wind ion charge exchange with ISM neutrals. A recent work focused on GJ 436 (M2.5, age: 7–11 Gyr; Saffe et al. 2005) suggests a relatively weak stellar wind, with $\dot{M} = 0.059^{+0.074}_{-0.040} \dot{M}_\odot$, using constraints from in-transit $\text{Ly}\alpha$ absorption due to an evaporating outflow from the exoplanet in this system (see Vidotto & Bourrier 2017).

Given the expected properties of its surface magnetic field (see Section 2.2), Barnard’s Star should in principle have an \dot{M} value lower¹² than Prox Cen, and similar to to GJ 436 (provided the similarities in spectral type and age). As our numerical models are consistent with both expectations, we consider that they provide a realistic representation of the stellar wind conditions around Barnard’s Star.

3.2. Wind Conditions at Barnard’s Star b

The semimajor axis and eccentricity of BSb are well constrained while its orbital inclination is not. As can be seen in

¹⁰ Defined as $M_A = U\sqrt{4\pi\rho}/B$, where U , ρ , and B , are the local values of the wind speed, density, and magnetic field strength, respectively.

¹¹ $\dot{M}_\odot \simeq 2 \times 10^{-14} \dot{M}_\odot \text{ yr}^{-1} = 1.265 \times 10^{12} \text{ g s}^{-1}$.

¹² Here we are implicitly assuming that \dot{M} scales proportionally to the activity/magnetic flux. While the winds of Sun-like stars seem to behave in this way (up to a certain level), this assumption is very uncertain in the case of M dwarf stars due to the lack of measurements (see Wood 2018).

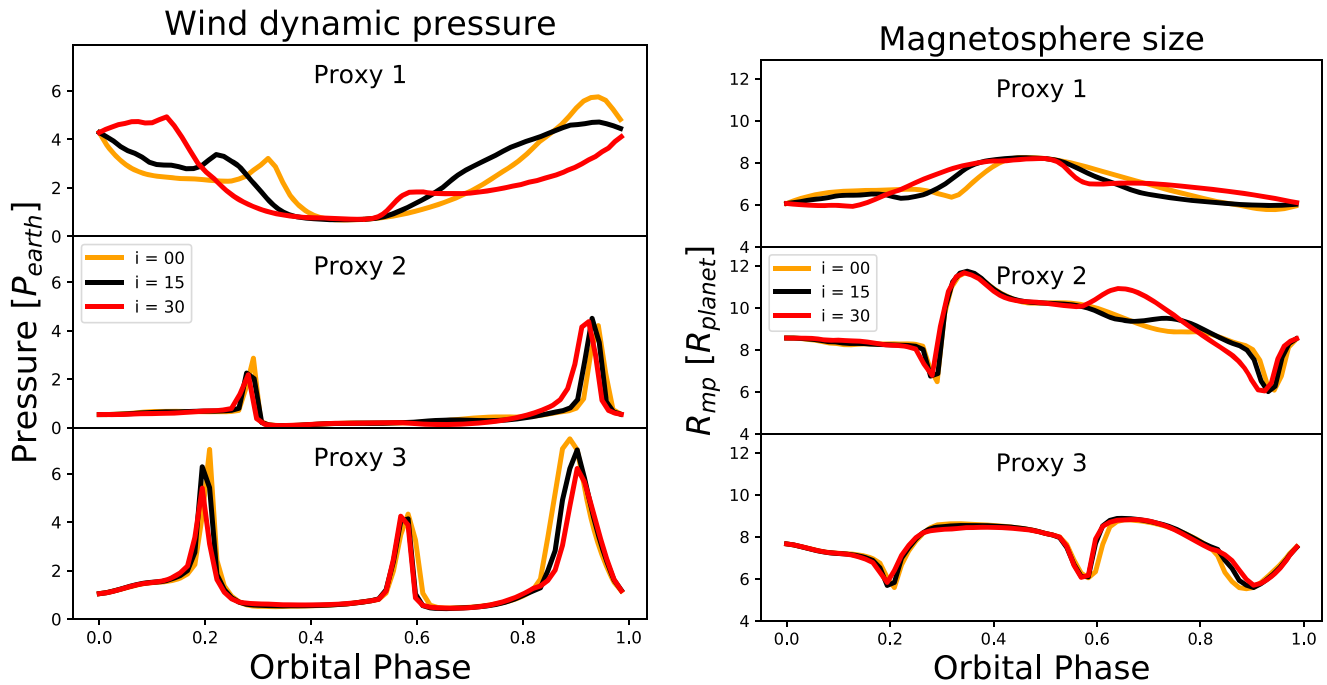


Figure 4. Behavior of P_{dyn} (left) and the magnetosphere size R_{mp} (right) along possible BSb orbits for each inclination in all of our proxies. The current sheet crossings appear as peaks (dips) in P_{dyn} (R_{mp}).

Figure 2, the stellar wind conditions vary quite strongly within the domain. The same occurs in the remaining two proxy simulations. To quantify this, we extract the wind dynamic pressure from a spheroid containing orbits at 0° , 15° , and 30° inclination angles (analogous to the ones shown in Figure 1, bottom panel), and construct a 2D latitude–longitude Mercator projection for each proxy (Figure 3). P_{dyn} can vary up to a factor of 100 (between 0.1 and 10.0 times the stellar wind conditions at Earth) for certain orbital inclinations. Changing the relative orientation of the orbit (i.e., the longitude of the ascending node) results in a different geometry of the 2D P_{dyn} projections, but their dynamic range is very similar.

In Figure 3 we also include the orbital paths for the three inclinations considered. We extract the wind pressure conditions along these orbits (see Figure 4, left panel) and use them to compute the size of a planetary magnetosphere as in Garraffo et al. (2016), assuming an Earth-like planetary magnetic field of ~ 0.3 G (right panel in Figure 4) and pressure equilibrium between the stellar wind and the planet’s magnetic field (e.g., Schield 1969; Gombosi 2004),

$$R_{\text{mp}}/R_{\text{planet}} = [B_p^2 / (8\pi P_{\text{SW}})]^{1/6}. \quad (1)$$

Here, R_{mp} is the radius of the magnetopause, R_{planet} is the radius of the planet, B_p refers to the planet’s equatorial magnetic field strength, and $P_{\text{SW}} = n_{\text{SW}} \cdot m_p \cdot U_{\text{SW}}^2$ is the ram pressure of the stellar wind.

For reference, the ram pressure of the ambient solar wind near Earth is typically about 1 nano Pascal (nPa). During the impact of a coronal mass ejection (CME), the number density lies in the range of $10\text{--}50 \text{ cm}^{-3}$, with speeds in the range of $500\text{--}2000 \text{ km s}^{-1}$, which translate to $1\text{--}5$ nPa for moderate CMEs and to $20\text{--}200$ nPa for the most extreme events (Lugaz et al. 2015).

In the case of BSb, the stellar wind pressure along the explored orbits, and for the considered proxy cases, ranges

between ~ 0.1 and ~ 7 times the solar wind pressure at 1 au. Assuming BSb has an Earth-like magnetic field, these wind conditions translate to a magnetospheric standoff radius of $\sim 6\text{--}12 R_{\text{planet}}$, compared to the Earth’s long-term average of $\sim 10 R_{\text{Earth}}$ (Pulkkinen 2007).

As can be seen from Figures 3 and 4, the conditions for the proxy 1 case are on average harsher than in the other two cases, but at the same time they change more slowly (in orbital phase). This situation translates directly to the magnetosphere size, which displays the least amount of variation along the orbits (Figure 4, right panel). The peaks of high pressure correspond to crossings of the current sheet, where the wind density is much higher. All orbits cross the current sheet, regardless of their inclination. Therefore, any orbit will be exposed to the higher pressures. It is good to note here that any given ZDI map case is only a snapshot of the field evolution that can occur on timescales of several days (active regions) to years (possible cycles). Therefore, the conditions inferred by our numerical models are intended to represent the mean values for a given system.

In addition to modeling three possible realistic scenarios for BSb, we have also simulated the wind for a magnetic field 10 times stronger in the proxy 1 case (GJ 51), which corresponds to 20% of that used for Proxima b in Garraffo et al. (2016). The results are similar in terms of geometry, differing over the domain by $\sim 40\%$ in the wind speed and by roughly one order of magnitude in \dot{M} and P_{dyn} . The magnetosphere size is reduced by $\sim 30\%$.

This is expected to some extent: the scaling of the absolute value of the surface magnetic field plays a secondary role influencing the space weather conditions far from the star at the orbit of BSb. Rather, the important factor is the wind density declining approximately as the inverse square of the orbital distance. Stronger magnetic flux will result in just slightly faster and more massive winds (see Garraffo et al. 2015; Réville et al. 2015; Alvarado-Gómez et al. 2016b).

As Barnard's Star is old, its wind will have been stronger in the past. The relative importance of such conditions on the planetary atmospheric evolution of BSb would be determined by the formation mechanism that took place in this system (i.e., migration or in situ). The inverse square scaling of wind density means a close-in planet will be surrounded by comparatively much more dense and fast varying plasma. This is what makes the expected space weather conditions on Proxima b and TRAPPIST-1 so dramatic. Not surprisingly, BSb, at 0.4 au, experiences much more mild conditions than close-in planets, and is comparable to days of bad space weather at Earth.

The prognosis for atmospheric survival on BSb is much brighter than predicted for Proxima b and the TRAPPIST-1 system.

The authors thank the referee for the helpful suggestions. J.D.A.G. and S.M. were supported by *Chandra* grants AR4-15000X and GO5-16021X, and HST grant GO-13754. J.J.D. was funded by NASA contract NAS8-03060 to the CXC and thanks the Director, Belinda Wilkes, for continuing advice and support. B.P.B. and J.S.O. were supported by NASA LWS grant NNX16AC92G. J.S.O. was supported by a Scialog Grant from the Research Corporation (ID #24231). O.C. was supported by NASA NExSS grant NNX15AE05G. This work used SWMF/BATSRUS tools developed at The University of Michigan Center for Space Environment Modeling. Simulations were performed on NASA's Pleiades cluster under award SMD-17-1330, provided by the NASA High-End Computing Program through the NASA Advanced Supercomputing Division at Ames Research Center.

Facility: NASA Pleiades Supercomputer.

Software: SWMF (Gombosi et al. 2018).

ORCID iDs

Julián D. Alvarado-Gómez  <https://orcid.org/0000-0001-5052-3473>

Cecilia Garraffo  <https://orcid.org/0000-0002-8791-6286>

Jeremy J. Drake  <https://orcid.org/0000-0002-0210-2276>

Benjamin P. Brown  <https://orcid.org/0000-0001-8935-219X>

Jeffrey S. Oishi  <https://orcid.org/0000-0001-8531-6570>

Sofia P. Moschou  <https://orcid.org/0000-0002-2470-2109>

Ofer Cohen  <https://orcid.org/0000-0003-3721-0215>

References

Alvarado-Gómez, J. D., Hussain, G. A. J., Cohen, O., et al. 2016a, *A&A*, **588**, A28
 Alvarado-Gómez, J. D., Hussain, G. A. J., Cohen, O., et al. 2016b, *A&A*, **594**, A95
 Benedict, G. F., McArthur, B., Nelan, E., et al. 1998, *AJ*, **116**, 429

Browning, M. K. 2008, *ApJ*, **676**, 1262
 Cohen, O., Drake, J. J., Gloer, A., et al. 2014, *ApJ*, **790**, 57
 Donati, J.-F., Semel, M., Carter, B. D., Rees, D. E., & Collier Cameron, A. 1997, *MNRAS*, **291**, 658
 Fares, R., Donati, J.-F., Moutou, C., et al. 2012, *MNRAS*, **423**, 1006
 Fares, R., Moutou, C., Donati, J.-F., et al. 2013, *MNRAS*, **435**, 1451
 Garraffo, C., Drake, J. J., & Cohen, O. 2015, *ApJL*, **807**, L6
 Garraffo, C., Drake, J. J., & Cohen, O. 2016, *ApJL*, **833**, L4
 Garraffo, C., Drake, J. J., Cohen, O., Alvarado-Gómez, J. D., & Moschou, S. P. 2017, *ApJL*, **843**, L33
 Garraffo, C., Drake, J. J., Dotter, A., et al. 2018, *ApJ*, **862**, 90
 Gombosi, T. I. 2004, *Physics of the Space Environment* (Cambridge: Cambridge Univ. Press)
 Gombosi, T. I., van der Holst, B., Manchester, W. B., & Sokolov, I. V. 2018, *LRSP*, **15**, 4
 Hünsch, M., Schmitt, J. H. M. M., Sterzik, M. F., & Voges, W. 1999, *A&AS*, **135**, 319
 Johnstone, C. P., Güdel, M., Brott, I., & Lüftinger, T. 2015a, *A&A*, **577**, A28
 Johnstone, C. P., Güdel, M., Lüftinger, T., Toth, G., & Brott, I. 2015b, *A&A*, **577**, A27
 Johnstone, C. P., Güdel, M., Stökl, A., et al. 2015c, *ApJL*, **815**, L12
 Kennedy, G. M., & Kenyon, S. J. 2008, *ApJ*, **673**, 502
 Lammer, H., Odert, P., Leitinger, M., et al. 2009, *A&A*, **506**, 399
 Lugaz, N., Farrugia, C. J., Huang, C.-L., & Spence, H. E. 2015, *GeoRL*, **42**, 4694
 Morbidelli, A., Lambrechts, M., Jacobson, S., & Bitsch, B. 2015, *Icar*, **258**, 418
 Morgenthaler, A., Petit, P., Morin, J., et al. 2011, *AN*, **332**, 866
 Morin, J., Donati, J.-F., Petit, P., et al. 2010, *MNRAS*, **407**, 2269
 Mulders, G. D., Pascucci, I., & Apai, D. 2015, *ApJ*, **814**, 130
 Petit, P., Dintrans, B., Solanki, S. K., et al. 2008, *MNRAS*, **388**, 80
 Pulkkinen, T. 2007, *LRSP*, **4**, 1
 Reiners, A. 2012, *LRSP*, **9**, 1
 Réville, V., Brun, A. S., Matt, S. P., Strugarek, A., & Pinto, R. F. 2015, *ApJ*, **798**, 116
 Ribas, I., Tuomi, M., Reiners, A., et al. 2018, *Natur*, **563**, 365
 Saffe, C., Gómez, M., & Chavero, C. 2005, *A&A*, **443**, 609
 Schield, M. A. 1969, *JGR*, **74**, 1275
 Schmitt, J. H. M. M., & Liefke, C. 2004, *A&A*, **417**, 651
 Semel, M. 1989, *A&A*, **225**, 456
 Sokolov, I. V., van der Holst, B., Manchester, W. B., et al. 2016, arXiv:1609.04379
 Stevenson, D. J., & Lunine, J. I. 1988, *Icar*, **75**, 146
 Toledo-Padrón, B., González Hernández, J. I., Rodríguez-López, C., et al. 2018, arXiv:1812.06712
 Tóth, G., van der Holst, B., Sokolov, I. V., et al. 2012, *JCoPh*, **231**, 870
 Trauger, J., Moody, D., Krist, J., & Gordon, B. 2016, *JATIS*, **2**, 011013
 van der Holst, B., Sokolov, I. V., Meng, X., et al. 2014, *ApJ*, **782**, 81
 Vidotto, A. A., & Bourrier, V. 2017, *MNRAS*, **470**, 4026
 Vidotto, A. A., Fares, R., Jardine, M., Moutou, C., & Donati, J.-F. 2015, *MNRAS*, **449**, 4117
 Vidotto, A. A., Jardine, M., Morin, J., et al. 2014, *MNRAS*, **438**, 1162
 Wargelin, B. J., & Drake, J. J. 2002, *ApJ*, **578**, 503
 Wood, B. E. 2018, *Journal of Physics Conference Series*, **1100**, 012028
 Wood, B. E., Linsky, J. L., Müller, H.-R., & Zank, G. P. 2001, *ApJL*, **547**, L49
 Wright, N. J., & Drake, J. J. 2016, *Natur*, **535**, 526
 Wright, N. J., Drake, J. J., Mamajek, E. E., & Henry, G. W. 2011, *ApJ*, **743**, 48
 Wright, N. J., Newton, E. R., Williams, P. K. G., Drake, J. J., & Yadav, R. K. 2018, *MNRAS*, **479**, 2351
 Yadav, R. K., Christensen, U. R., Morin, J., et al. 2015, *ApJL*, **813**, L31